Plasma Sources
Science and
Technology

PURPOSE-LED
PUBLISHING™

LETTER • **OPEN ACCESS**

Optical interferometry of high-energy nanosecond pin-to-pin discharges in atmospheric air

To cite this article: Nicholas Babusis *et al* 2025 *Plasma Sources Sci. Technol.* **34** 01LT04

View the article online for updates and enhancements.

You may also like

- Active learning-guided exploration of parameter space of air plasmas to enhance the energy efficiency of NO_x production
Ketong Shao, Xuekai Pei, David B Graves et al.
- Simulation of a pulsed CO_2 plasma based on a six-temperature energy approach
I Tsonev, O Biondo and A Bogaerts
- Time-resolved diagnostics of a pin-to-pin pulsed discharge in water: pre-breakdown and breakdown analysis
C Rond, J M Desse, N Fagnon et al.

This content was downloaded from IP address 192.107.175.1 on 19/12/2025 at 19:41

OPEN ACCESS
IOP Publishing

Letters
Plasma Sources Science and Technology

Plasma Sources Sci. Technol. **34** (2025) 01LT04 (7pp)
https://doi.org/10.1088/1361-6595/adae30

Letter

Optical interferometry of high-energy nanosecond pin-to-pin discharges in atmospheric air

Nicholas Babusis, Won Joon Jeong and Alexey Shashurin*

School of Aeronautics and Astronautics, Purdue University, West Lafayette, IN, United States of America

E-mail: ashashur@purdue.edu

Received 16 October 2024, revised 23 December 2024
Accepted for publication 24 January 2025
Published 31 January 2025

Abstract

This paper describes the construction and application of an optical-frequency Michelson interferometer for measuring electron number density within high-energy, high-power nanosecond pin-to-pin discharges (>10 mJ pulse energy, >1 MW pulse power). A 21 mJ, 11 ns spark across a 3 mm pin-to-pin electrode gap was analyzed at 7 ns into the discharge to demonstrate the operation of the interferometer. A peak electron density of 2.3×10^{17} cm^{-3} was observed at these conditions, and it was consistent with estimates of plasma channel resistance based on V–I measurements. This initial work paves the way for a larger parametric study of the spatial and temporal dynamics of electron number density in nanosecond pin-do-pin discharges under various conditions.

Keywords: optical interferometry, nanosecond discharges, electron number density, plasma diagnostics, nanosecond sparks

Nanosecond discharges have received much attention in recent years motivated by their relevance to a wide range of fields such as plasma-assisted combustion [1], flow control [2, 3], electronic switching [4, 5], and chemical processing [6]. High-energy pin-to-pin discharges are of particular interest to plasma-assisted combustion due to the efficient heating of gas within the discharge, enabling ignition of lean fuel/air mixtures with reduced NO_x combustion products [7, 8].

Multiple studies have explored ns-discharges at relatively low pulse energies and powers (<10 mJ pulse energy, <1 MW pulse power). For example, coherent microwave scattering has been employed to measure electron densities up to $\sim 10^{16}$ cm^{-3} in 5 mJ, 90 ns (0.056 MW) pin-to-pin discharges [9, 10]. Gas dynamics of pin-to-pin ns discharges have been studied extensively via Schlieren imagine and laser-induced fluorescence such as in [11–13]. (1–6 mJ, 10 ns, 0.1–0.6 MW).

However, relatively few studies exist for high-energy nanosecond pin-to-pin discharges (>10 mJ pulse energy, >1 MW pulse power). These high-energy discharges create extreme conditions within the spark channel that lead to high temperatures and ionization degrees [7, 14], as well as ultrafast heating and hydrodynamic expansion [13, 15]. Plasma parameters of high-energy dielectric barrier discharges in pure nitrogen have been studied for 20 ns, 6–30 mJ (0.3–1.5 MW) discharge pulses, reporting electron densities up to 5×10^{18} cm^{-3} via Stark broadening of the H_α line [15]. Similarly, [7, 16] investigated plasma properties in a 54 mJ, 25 ns (2.2 MW) pin-to-pin discharge, measuring electron densities up to 10^{19} cm^{-3}

* Author to whom any correspondence should be addressed.

Original content from this work may be used under the terms of the Creative Commons Attribution 4.0 licence. Any further distribution of this work must maintain attribution to the author(s) and the title of the work, journal citation and DOI.

© 2025 The Author(s). Published by IOP Publishing Ltd

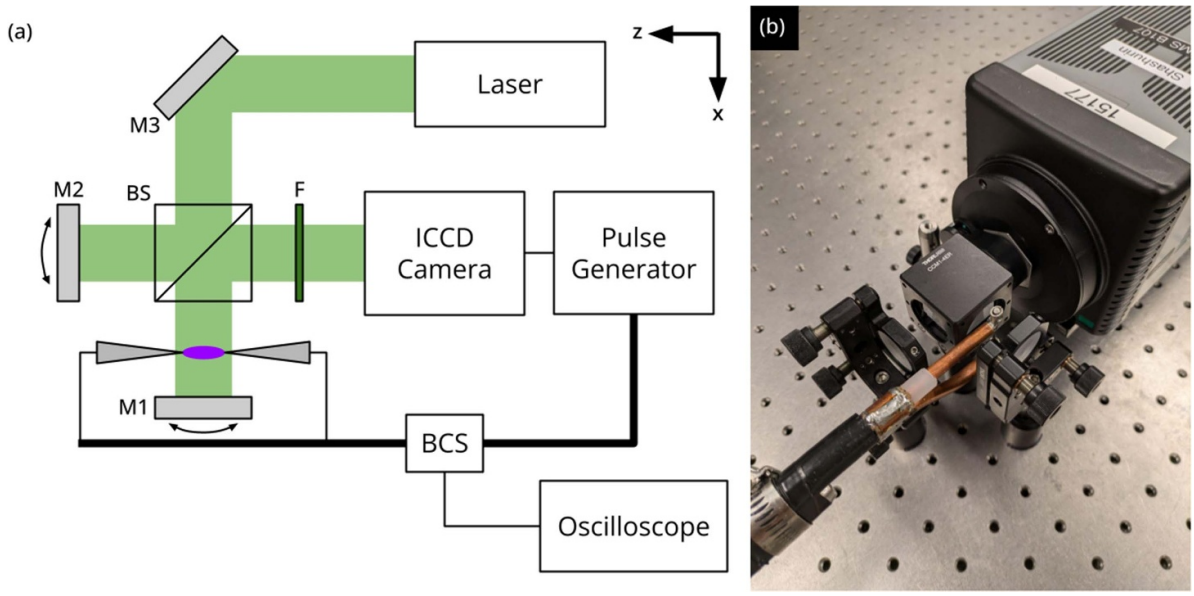

Figure 1. (a) Experiment schematic and (b) photo of the laser interferometry system.

extracted from Stark broadening of the N+ lines. A detailed comparison of low-energy and high-energy nanosecond discharges can be found in [17].

Undoubtedly, electron number density (n_e) is one of the most important parameters that governs plasma dynamics of the high-energy nanosecond pin-to-pin discharges. As discussed above, previous works suggest that high electron number densities exceeding 10^{17} cm^{-3} can be expected for these discharges. The coherent microwave scattering cannot be applied to measure $n_e > 10^{17}$ cm^{-3} due to the skin effect limitation [18], while optical interferometry offers an attractive opportunity to measure n_e in that range with good spatial and temporal resolution. Specifically, optical interferometry has been successfully used to map femtosecond laser filaments with n_e in the range 10^{16}–10^{17} cm^{-3} and comparable plasma channel diameters of ∼100–200 μm [19]. The electron number densities $n_e \sim 10^{16}$ cm^{-3} were reported as the lower detection limit due to the small optical phase shift, while higher n_e values produce larger phase shifts, making them easier to detect. Therefore, utilization of optical interferometry for high energy ns-discharges with expected $n_e > 10^{17}$ cm^{-3} and plasma channel diameters of about 100 s of μm should be feasible.

Therefore, electron number densities have been extensively characterized for low-energy ns-discharges (<10 mJ energy, <1 MW power). However, spatially and temporally resolved measurements of high energy pin-to-pin ns-discharges (>10 mJ and >1 MW) is very limited. This paper describes the initial development of optical interferometry to diagnose high-energy ns-discharges.

The experiment consisted of a pin-to-pin spark gap within one arm of a Michelson interferometer as shown in figure 1. A CW 532 nm diode laser was placed sufficiently far from the experiment to allow the beam to expand to a convenient diameter due to the natural divergence of the beam. A 50/50 beam splitter divided the beam into probe and reference arms and combined the reflected beams. A slight angular offset of the reference beam in the x–z plane was introduced by adjusting M2 in order to create a vertical fringe pattern of the desired frequency. A 532 nm line filter F was used to filter out white light emissions from the spark. A Princeton Instruments PiMax 4 ICCD camera was utilized to record the interferogram after being triggered from the pulse generator.

The relatively large refractive index gradient presented by the spark required minimizing the distance traveled by the laser beam between the spark and ICCD to minimize deflection of the probe beam. The distance traveled by the probe beam after its first pass through plasma was about 97 mm. The temporal resolution of the interferometer was limited to 3 ns corresponding to the minimal exposure time of the ICCD camera. ICCD delay timing was correlated with the plasma discharge by observing the white light emissions from the spark (filter removed and laser off) and defining the delay when emissions were visible in 50% of exposures as the $t = 0$ time.

The nanosecond discharge was generated by a FPG 20-50NS10 pulse generator (11.1 ns FWHM square wave pulse, 40.1 mJ forward pulse energy, 1 Hz repetition rate) between a pair of tungsten pin electrodes separated by a 3 mm air gap [17], as shown in figure 2(a). The pulse from the pulse generator traveled to the spark gap via a RG217 coaxial cable (50 Ω impedance), with 25 m of cable length between the pulser and BCS (back-current shunt), and 5 m of cable length between the BCS and the spark gap assembly. Electrical characteristics of the discharge are shown in figures 2(b) and (c). Waveforms of the discharge voltage and current were evaluated from the forward and reflected current pulses (I_f and I_r, respectively) measured by the BCS as follows: $I_d = I_f + I_r$ and $V_d = \frac{I_f - I_r}{Z_0}$ (more details on the circuit and electrical measurements are provided in Jeong *et al* [17]). The pulse energy of $E_d = 20.8$ mJ

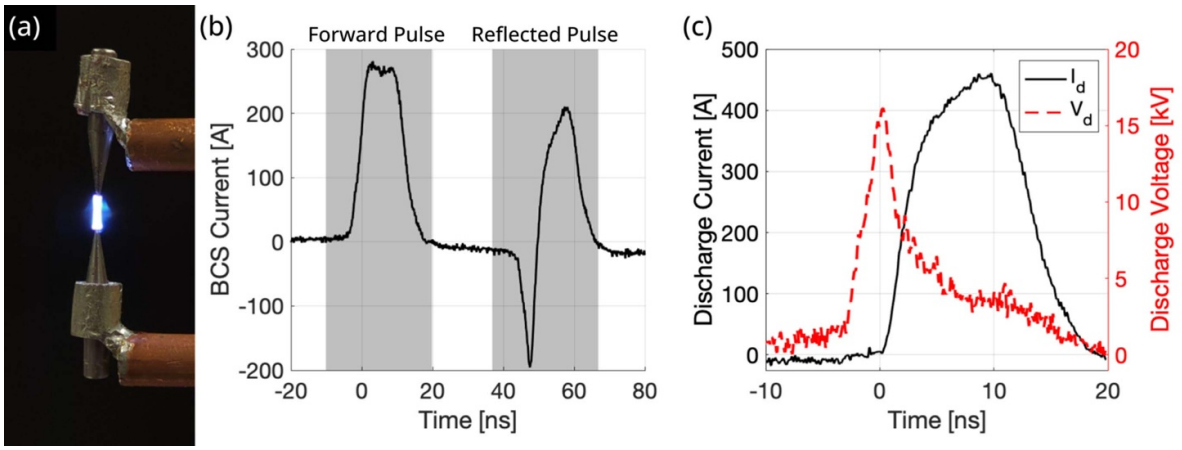

Figure 2. (a) Photograph of the ns-discharge. (b) Typical raw signal of forward and reflected current pulses measured by the BCS. (c) Typical discharge current and discharge voltage waveforms of ns-discharge.

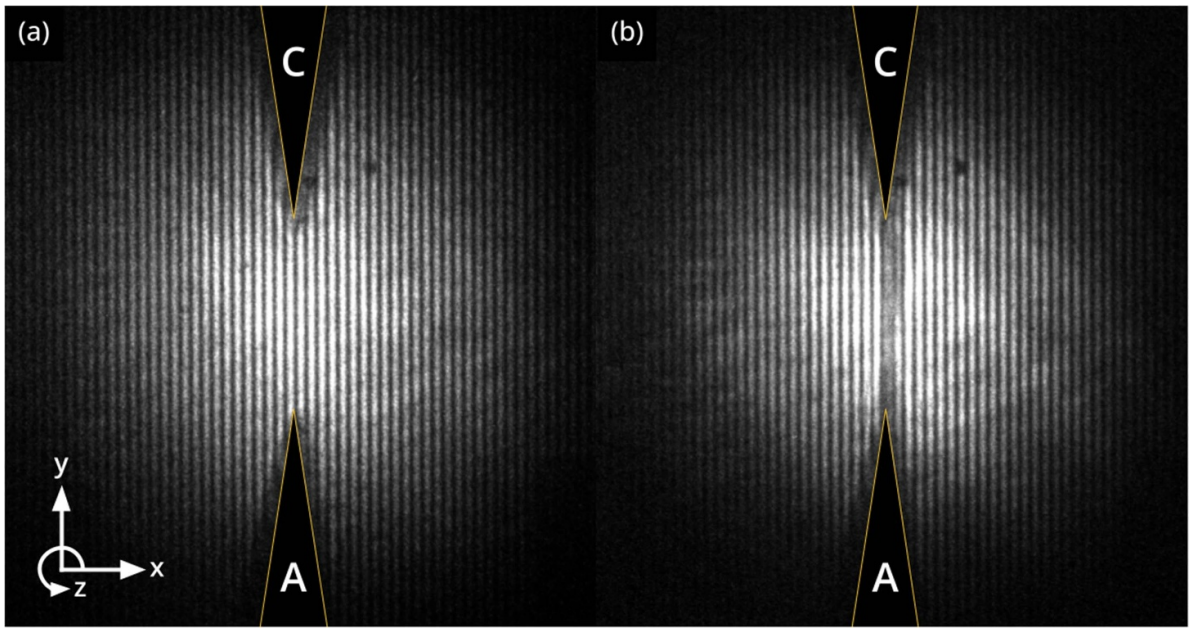

Figure 3. Typical interferograms (a) before the breakdown and (b) at 7 ns after breakdown.

was derived via integration of the V_d and I_d traces as $\int I_d V_d dt$. The spark was fairly reproducible between discharge pulses, as evidenced by a stable spark location within ± 12 μm and minimal discharge current variations of $\pm 4\%$. No visible signs of erosion or oxidation were observed on the electrodes throughout the experiment.

Typical interferograms with and without the ns-discharge are shown in figure 3. Fringes were directed parallel to the discharge axis to provide a nonzero background frequency for horizontal slices of the image. This allows differentiation between phase shifts and experimental noise, which was strongest at low spatial frequencies. The fringe density of 6 fringes/mm (14 pixels per fringe) was chosen empirically to minimize noise in the phase shift profile.

Interferograms were processed into phase shift profiles using the FFT-based procedure described in Takeda *et al* [20] and illustrated in figure 4. First, a region of the interferogram was selected for analysis, as shown in figure 4(a). The intensity profile was averaged along the vertical direction and Fourier-transformed along the horizontal direction (see figure 4(b)). The Fourier transform was then shifted by the frequency of the unperturbed fringes f_0 and trimmed in order to capture only the slight perturbations in the vicinity of f_0 caused by phase shifts, as shown in figure 4(c). Finally, an inverse FFT was applied to obtain a phase shift profile. This process was repeated and averaged over 40 images both with and without the discharge present. The background discharge-off phase profile was subtracted from the corresponding discharge-on profile to create the final phase shift profile illustrated in figure 4(d). Note that the phase profile in figure 4(d) is referred to as $2\phi\,(x)$ to account for double passage of the interferometer's laser beam through the plasma column. Extraction of phase shifts

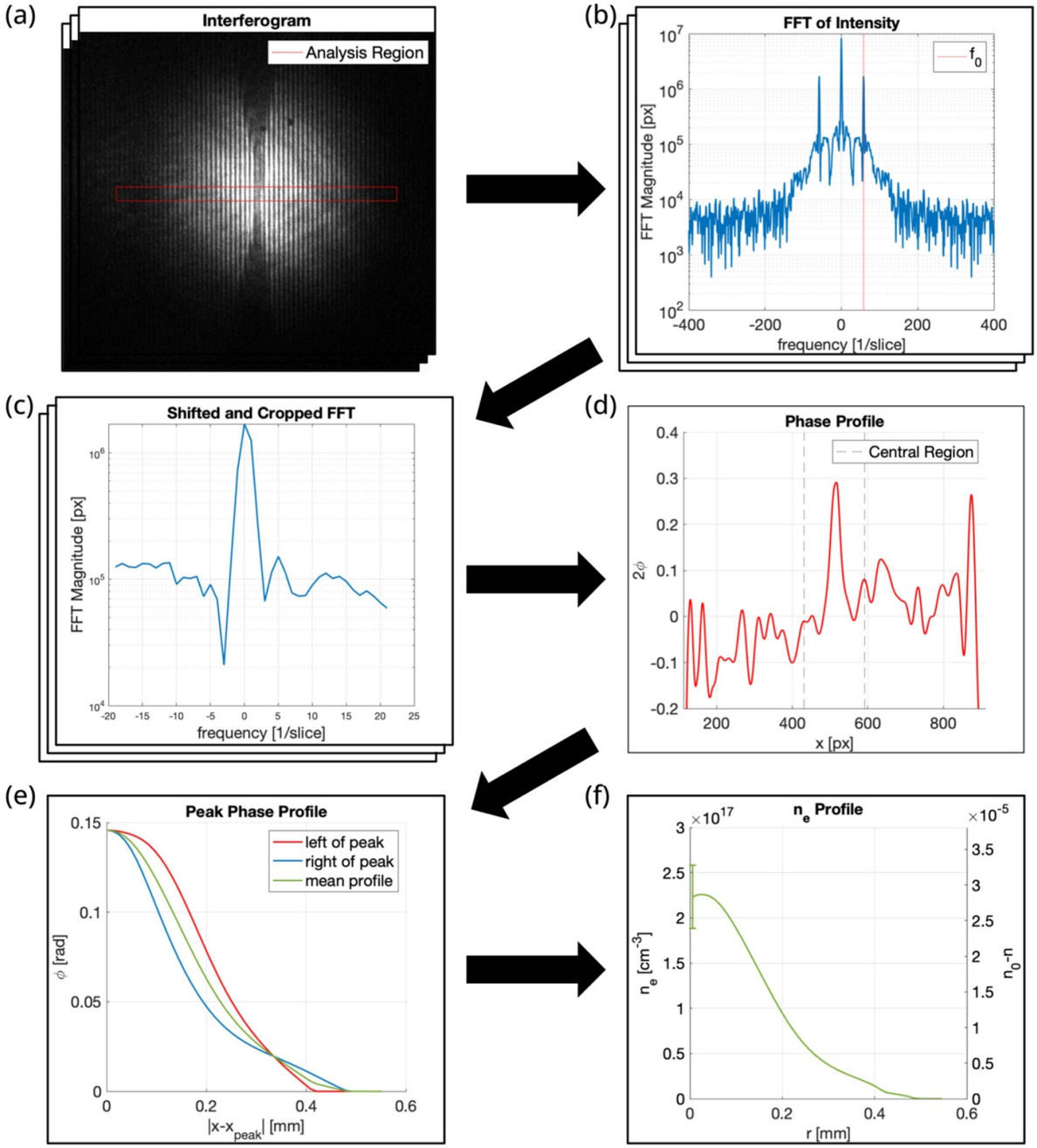

Figure 4. Algorithm for extracting radial electron density profiles from interferograms.

for electron density analysis was restricted to a central region (2 mm wide along x-axis) of the phase profile where phase noise is minimized.

The left and right wings of the phase shift peak were then averaged to create a mean phase shift profile on a single laser passage $\phi\,(x)$, as shown in figure 4(e). Note that generation of plasma in the gap is expected to slightly reduce the refractive index in comparison with that of the ambient air (n_0) as follows: $n = n_0 - \frac{\omega_p^2}{2\omega^2}$, where ω_p is the plasma frequency and ω is the laser frequency (the electron collision frequency, $\nu \sim 10^{12}$ s^{-1}, is neglected in comparison with the laser frequency, $\sim 10^{15}$ Hz, in the refractive index expression) [9, 21]. Therefore, the positive phase shift $\phi\,(x) = \frac{2\pi}{\lambda}\int_{-\infty}^{\infty}(n_0 - n)\mathrm{d}z$ is to be expected, which is consistent with the experimental results shown in figures 4(d) and (e).

One can see that, according to equation (1), the phase profile $\phi\,(x)$ is correlated with the term $\frac{2\pi}{\lambda}\,(n_0 - n\,(r))$ via Abel transform. Therefore, the variation of refractive index due to the plasma $(n_0 - n)$ can be obtained using Abel inversion according to equation (2):

$$\phi\,(x) = \frac{2\pi}{\lambda}\int_{-\infty}^{\infty}(n_0 - n)\,\mathrm{d}z = 2\int_{x}^{\infty}\frac{\frac{2\pi}{\lambda}\,(n_0 - n)\,r\mathrm{d}r}{\sqrt{r^2 - x^2}} \qquad (1)$$

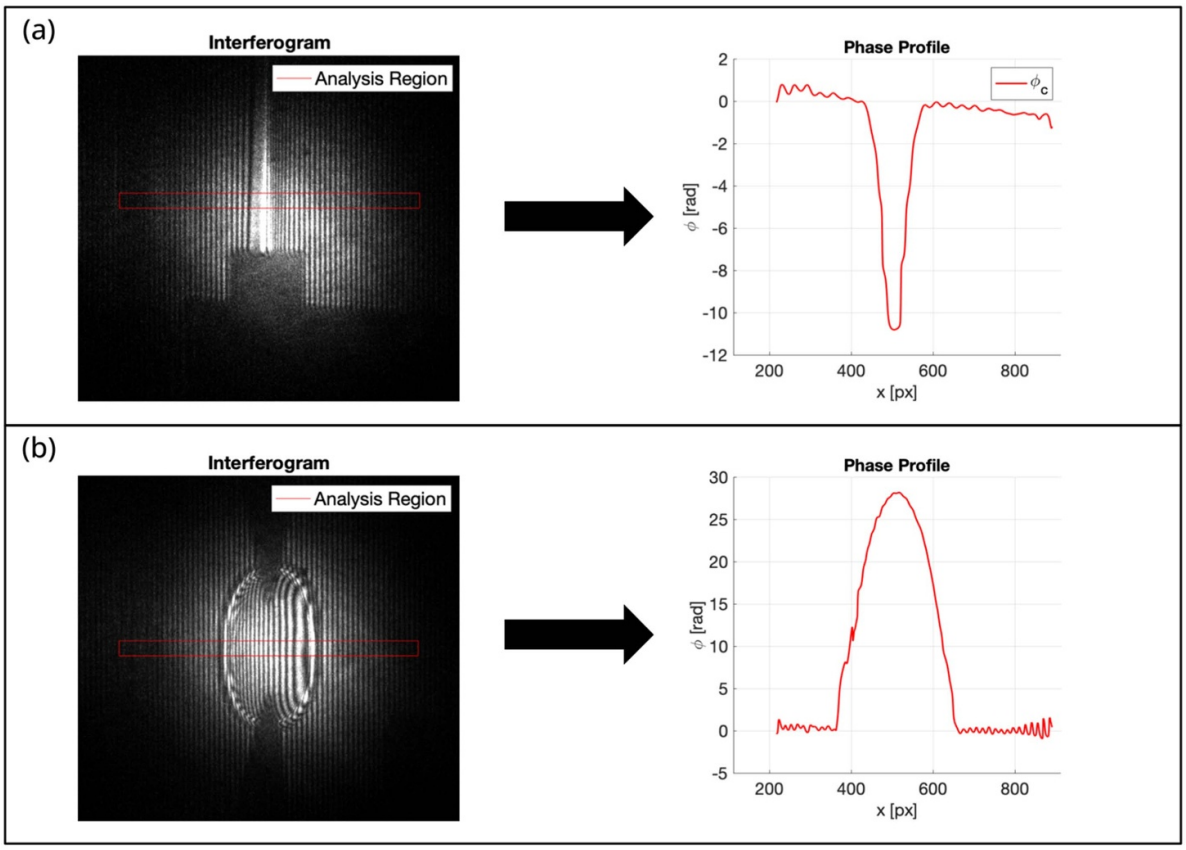

Figure 5. Interferogram and phase shift profile of (a) high-refractive index gas jet and (b) late stages of plasma discharge ($t = 1.28$ μs) associated with reduced refractive index.

$$n_0 - n = -\frac{\lambda}{2\pi^2}\int_r^\infty \frac{\mathrm{d}\phi}{\mathrm{d}x}\frac{\mathrm{d}x}{\sqrt{x^2 - r^2}}. \tag{2}$$

Finally, the electron number density profile $n_e(r)$ can be determined using the expressions for the refractive index of plasma $n = n_0 - \frac{\omega_p^2}{2\omega^2}$ and plasma frequency $\omega_p = \frac{e^2 n_e}{\varepsilon_0 m_e}$, where e is the electron charge, m_e is the electron mass, and ε_0 is the dielectric permittivity of vacuum. Correspondingly, the electron number density profile $n_e(r)$ plotted in figure 4(f) was determined as follows:

$$n_e(r) = \frac{2\varepsilon_0 m_e \omega^2}{e^2}(n_0 - n) = -\frac{2\varepsilon_0 m_e c\omega}{\pi e^2}\int_r^\infty \frac{\mathrm{d}\phi}{\mathrm{d}x}\frac{\mathrm{d}x}{\sqrt{x^2 - r^2}}. \tag{3}$$

A peak electron number density of 2.3×10^{17} cm^{-3} (about 1% ionization degree) within about 360 μm FWHM diameter plasma channels was observed. It is important to note that these n_e-values yield consistent estimation of the plasma channel resistance (R_c). Specifically, R_c can be estimated based on the measured n_e-values as follows: $R_c = \frac{L}{\sigma S}$, where L is the gap size ($L = 3$ mm), $S = \frac{\pi D_p^2}{4}$ is the area of the plasma channel, D_p is the plasma channel diameter ($D_p \sim 360$ μm), $\sigma = \frac{\varepsilon_0 \omega_p^2}{\nu}$ is the plasma conductivity, and $\omega_p = \frac{e^2 n_e}{\varepsilon_0 m_e}$ is the plasma frequency. Finally, this yields $R_c \sim 10$ Ω based on the $n_e \sim 10^{17}$ cm^{-3} reported in this work. From the other hand, R_c can be roughly estimated via *V–I* measurements in figure 2(a) to be about $R_c \sim 9$ Ω ($\sim 3800\,\mathrm{V}/\sim 430\,\mathrm{A}$ at $t = 7$ ns). Therefore, both R_c values extracted from the electron number density measured here and from *V–I* measurements are consistent. It must be noted that significantly higher electron number densities of about $\sim 10^{19}$ cm^{-3} have been reported in comparable experimental conditions (pin-to-pin spark, 3 mm gap, 54 mJ pulse energy, 25 ns pulse duration) [7]. These high values of $n_e \sim 10^{19}$ cm^{-3} would result in phase shifts significantly larger than those observed experimentally in this work.

To further validate the interferometer developed here, we confirmed that the sign of the measured phase shift was accurate for two different non-plasma objects. First, a jet of high refractive index gas (HFO-1234ze) from a gas duster bottle was used to model locally increased refractive index: $n > n_0$ [22]. Therefore, a negative phase shift $\phi = \frac{2\pi}{\lambda}\int_{-\infty}^{\infty}(n_0 - n)\mathrm{d}z$ is to be expected, which was confirmed by the measurements presented in figure 5(a). Second, we analyzed the late post-discharge stage of the considered here nanosecond spark, after the plasma has decayed. This stage is associated with reduced gas number density in the electrode axis vicinity due to expansion of the heated gas [9]. Correspondingly, reduced refractive index ($n < n_0$) and a positive phase shift is expected [23], which was confirmed by the corresponding measurements presented in figure 5(b).

The measurement error of n_e-values reported here is associated with the interferometer system, data processing procedure, and variability of the plasma spark (both temporal and spatial), and was determined to be 3.5×10^{16} cm^{-3} (10 trials at identical conditions were evaluated). This measurement error was governed by the corresponding phase noise of the measured interferograms, which, in turn, was associated with several factors including intensity noise and discretization effects introduced by the ICCD camera, laser stability, and mechanical vibrations of the system. The dominant contribution to this phase noise was determined to be the intensity noise introduced by the ICCD camera based on modeling of effects introduced by these factors using computer-simulated interferograms. The typical phase noise was determined to be ± 0.03 radians by analysis of pre-discharge images, when no phase shift is expected. The LI system developed here can be utilized for n_e-measurements in sub-mm plasma channels with relatively high electron density ($>3.5 \times 10^{16}$ cm^{-3}), such as in nanosecond sparks and laser-induced plasmas. The measurement errors can be substantial when testing sub-mm plasma channels with $n_e < 10^{17}$ cm^{-3}; however, for $n_e > 10^{17}$ cm^{-3}, significant and easily detectable phase shifts occur, ensuring reliable n_e-measurements with minimal errors.

It is important to consider the applicability limits of the developed here diagnostic method as multiple factors besides n_e can affect the refractive index of the plasma object. These factors include air heating by the discharge pulse and associated air displacement from the spark vicinity, dissociation of air constituents, and refraction of the interferometer's laser beam on the spark channel. The contributions of each mechanism and corresponding applicability limits of the interferometer developed here are discussed below.

First, the discharge pulse causes very fast air heating, leading to the displacement of air from the spark region. This displacement reduces the local air density in the spark vicinity, ultimately altering the refractive index. This process limits applicability of the diagnostic method developed here to the first 20 ns of the discharge, while gas displacement is still minimal. For times $t > 0$ ns, isolating the effects of gas heating and displacement from the influence of n_e becomes unfeasible. This limitation can be justified by estimating the characteristic times of gas displacement through analysis of the shockwave propagation. For the purpose of estimating shockwave velocity, the spark was assumed to instantaneously and uniformly deposit its energy into a 360 μm diameter cylinder, heating the gas to $\sim$56 000 K. Using normal shock relations, an initial shockwave propagation velocity of 10 600 m s^{-1} can be estimated (traversing the plasma radius in $\sim$17 ns) while visual observations of the shock determined an average velocity of $\sim$1400 m s^{-1} averaged over the first μs of the discharge. This indicates that air density perturbation in the spark channel due to shockwave is expected on times $>$20 ns.

Second, dissociation products created during the ns-discharge can affect the refractive index for times $t > 100$ ns, so that the technique proposed here can only be utilized during the initial stage of the discharge ($t < 100$ ns). Pokharel *et al* [24] reported that dissociation of the nitrogen molecules can produce substantial change of the refractive index (e.g. full dissociation of nitrogen can reduce refraction index by $\Delta n \sim -8 \times 10^{-5}$ which is comparable to the reduction due to free electrons $\Delta n \sim -3 \times 10^{-5}$ measured here, as shown in figure 4(f)). However, previous works indicate that dissociation of oxygen due to quenching of electronically excited states of nitrogen by O_2 can be expected for $t > 100$ ns after the discharge, while post-discharge nitrogen dissociation is negligible [16, 25]. Finally, note that dissociation produces a contribution to the phase shift of the same sign as free electrons, so, if significant, it would lead to overestimating the n_e values.

Third, refraction of the laser beam on the spark channel and associated deflection of rays while propagating through the plasma is expected to be important for dense plasma channels while negligible for the plasma channels considered in this work. The maximum phase shift gradient of 1.1 rad mm^{-1} observed in figure 4(e) creates a wavefront deflection angle after passing the plasma channel of about $\theta = \frac{\lambda}{2\pi}\frac{\partial \phi}{\partial x} = 0.005°$. This corresponds to a lateral deflection of $\sim$10 μm at the ICCD sensor, which is substantially less than the plasma radius and can be neglected. This conclusion was validated experimentally by blocking the reference beam and observing only small variations in the flatfield image when the plasma was introduced.

In the future, the authors intend to use this methodology to perform comprehensive parametric study of the spatial and temporal dynamics of electron number density in nanosecond pin-do-pin discharges under various conditions including different gap sizes, pulse energies, repetition frequencies, etc. Potential improvements to the experimental setup include the use of femtosecond laser gating for improved temporal resolution, improvement of the imaging system SNR, or the use of multiple laser frequencies for discrimination between the effects of plasma and other refractive index contributions.

In conclusion, the interferometer and data processing algorithm described above demonstrated the ability to extract radial electron number density profiles of high-energy, high-power nanosecond pin-to-pin discharges in atmospheric air ($>$10 mJ pulse energy, $>$1 MW average pulse power). The observed electron density of 2.3×10^{17} cm^{-3} in the center of the 3 mm gap filament excited by 21 mJ, 11 ns nanosecond pulse was consistent with estimates of plasma channel resistance based on *V–I* measurements. Analysis of competing influences of various factors on the refractive index determined that the technique is applicable during the initial 10 s of nanoseconds of the discharge when local change of air density in the spark vicinity and dissociation of air constituents is negligible.

Data availability statement

The data that support the findings of this study are openly available at the following URL/DOI: http://doi.org/10.17605/OSF.IO/A56BG.

Acknowledgment

The authors would like to thank M N Shneider, A Y Starikovskiy, A Dogariu, and A Morozov for valuable discussions. This work was supported by the U.S. Department of Energy (Grant No. DE SC0023209).

ORCID iDs

Nicholas Babusis https://orcid.org/0009-0008-5943-6665
Alexey Shashurin https://orcid.org/0000-0003-2980-8954

References

[1] Starikovskaia S M 2014 Plasma-assisted ignition and combustion: nanosecond discharges and development of kinetic mechanisms *J. Phys. D: Appl. Phys.* **47** 353001
[2] Bayoda K D, Benard N and Moreau E 2015 Nanosecond pulsed sliding dielectric barrier discharge plasma actuator for airflow control: electrical, optical, and mechanical characteristics *J. Appl. Phys.* **118** 063301
[3] Roupassov D V, Nikipelov A A, Nudnova M M and Starikovskii A Y 2009 Flow separation control by plasma actuator with nanosecond pulsed-periodic discharge *AIAA J.* **47** 168–85
[4] Levko D and Raja L L 2015 Early stage time evolution of a dense nanosecond microdischarge used in fast optical switching applications *Phys. Plasmas* **22** 123518
[5] Huang J, Liu Z, Chen J and Li H 2023 Study on gas spark discharge plasma diagnosed by laser interferometric technology *J. Mater. Process. Des.* **7** 49–58
[6] Scapinello M, Martini L M, Dilecce G and Tosi P 2016 Conversion of CH_4/CO_2 by a nanosecond repetitively pulsed discharge *J. Phys. D: Appl. Phys.* **49** 075602
[7] Lo A, Cessou A, Lacour C, Lecordier B, Boubert P, Xu D A, Laux C O and Vervisch P 2017 Streamer-to-spark transition initiated by a nanosecond overvoltage pulsed discharge in air *Plasma Sources Sci. Technol.* **26** 045012
[8] Starikovskiy A and Aleksandrov N 2013 Plasma-assisted ignition and combustion *Prog. Energy Combust. Sci.* **39** 61–110
[9] Wang X, Patel A and Shashurin A 2021 Combined microwave and laser Rayleigh scattering diagnostics for pin-to-pin nanosecond discharges *J. Appl. Phys.* **129** 183302
[10] Wang X, Patel A, Bane S and Shashurin A 2021 Experimental study of atmospheric pressure single-pulse nanosecond discharge in pin-to-pin configuration *J. Appl. Phys.* **130** 103303
[11] Xu D A, Lacoste D A and Laux C O 2016 Ignition of quiescent lean propane–air mixtures at high pressure by nanosecond repetitively pulsed discharges *Plasma Chem. Plasma Process.* **36** 309–27
[12] Dumitrache C, Gallant A, Minesi N, Stepanyan S, Stancu G D and Laux C O 2019 Hydrodynamic regimes induced by nanosecond pulsed discharges in air: mechanism of vorticity generation *J. Phys. D: Appl. Phys.* **52** 364001
[13] Stepanyan S, Minesi N, Tibere-Inglesse A, Salmon A, Stancu G D and Laux C O 2019 Spatial evolution of the plasma kernel produced by nanosecond discharges in air *J. Phys. D: Appl. Phys.* **52** 295203
[14] Ding C, Khomenko A Y, Shcherbanev S A and Starikovskaia S M 2019 Filamentary nanosecond surface dielectric barrier discharge. Experimental comparison of the streamer-to-filament transition for positive and negative polarities *Plasma Sources Sci. Technol.* **28** 085005
[15] Shcherbanev S A, Ding C, Starikovskaia S M and Popov N A 2019 Filamentary nanosecond surface dielectric barrier discharge. Plasma properties in the filaments *Plasma Sources Sci. Technol.* **28** 065013
[16] Lo A, Cessou A and Vervisch P 2014 Space and time analysis of the nanosecond scale discharges in atmospheric pressure air: II. Energy transfers during the post-discharge *J. Phys. D: Appl. Phys.* **47** 115202
[17] Jeong W J, Shashurin A, Dogariu A, Starikovskiy A Y, Morozov A and Shneider M 2024 Characterization of high-energy nanosecond single-pulse discharges in pin-to-pin configuration *AIAA SciTech Forum and Exposition 2024* (American Institute of Aeronautics and Astronautics Inc)
[18] Shashurin A, Patel A R, Wang X, Sharma A and Ranjan A 2023 Coherent microwave scattering for diagnostics of small plasma objects: a review *Phys. Plasmas* **30** 063508
[19] Bodrov S, Bukin V, Tsarev M, Murzanev A, Garnov S, Aleksandrov N and Stepanov A 2011 Plasma filament investigation by transverse optical interferometry and terahertz scattering *Opt. Express* **19** 6829–35
[20] Takeda M, Ina H and Kobayashi S 1982 Fourier-transform method of fringe-pattern analysis for computer-based topography and interferometry *J. Opt. Soc. Am.* **72** 156
[21] Raizer Y 1991 *Gas Discharge Physics* 1st edn (Springer)
[22] Sampson C C, Kamson M, Hopkins M G, Stanwix P L and May E F 2019 Dielectric permittivity, polarizability and dipole moment of refrigerants R1234ze(E) and R1234yf determined using a microwave re-entrant cavity resonator *J. Chem. Thermodyn.* **128** 148–58
[23] Stone J and Zimmerman J 2001 Index of refraction of air (NIST Engineering Metrology Toolbox) (available at: https://www.nist.gov/publications/index-refraction-air)
[24] Pokharel S, Dogariu A, Miles R and Tropina A 2024 Refractive index modification induced by femtosecond laser filament *AIAA SciTech Forum and Exposition 2024* (American Institute of Aeronautics and Astronautics Inc)
[25] Popov N A 2016 Pulsed nanosecond discharge in air at high specific deposited energy: fast gas heating and active particle production *Plasma Sources Sci. Technol.* **25** 044003